ACADÉMIE
DES SCIENCES
INSTITUT DE FRANCE

Comptes Rendus
Mécanique

Giulio Sanna, Mario Pistis, Victor Eremeyev, Salma Barboura and Mario Spagnuolo

Mechanical stabilization of filament-printed fibrous metamaterials via novel hinge architectures

Volume 354 (2026), p. 761-782

Online since: 28 August 2026

https://doi.org/10.5802/crmeca.380

CENTRE
MERSENNE

The Comptes Rendus. Mécanique *are a member of the*
Mersenne Center for open scientific publishing
www.centre-mersenne.org — e-ISSN : 1873-7234

ACADÉMIE
DES SCIENCES
INSTITUT DE FRANCE

Comptes Rendus. Mécanique
2026, Vol. 354, p. 761-782
https://doi.org/10.5802/crmeca.380

Research article

Mechanical stabilization of filament-printed fibrous metamaterials via novel hinge architectures

Giulio Sanna [a], **Mario Pistis** [a], **Victor Eremeyev** [a], **Salma Barboura** [b] **and Mario Spagnuolo** [*, a, c]

[a] Department of Civil and Environmental Engineering and Architecture (DICAAR), University of Cagliari, Cagliari, Italy

[b] LSPM, University Sorbonne Paris Nord, UPR-CNRS 3407, 99 avenue Jean Baptiste Clement, Villetaneuse 93430, France

[c] International Research Center for the Mathematics and Mechanics of Complex Systems (M&MoCS), University of L'Aquila, L'Aquila, Italy

E-mails: g.sanna90@studenti.unica.it (G. Sanna), mario.pistis@unica.it (M. Pistis), victor.eremeev@unica.it (V. Eremeyev), salma.barboura@univ-paris13.fr (S. Barboura), mario.spagnuolo@unica.it (M. Spagnuolo)

Abstract. Fibrous metamaterials derive their macroscopic mechanical response from the interplay between fiber deformation and hinge mechanics. This work introduces a novel printable hinge conception for filament-based additive manufacturing that is designed to behave as a perfect pivot and to improve structural stability under compression. Experiments on specimens subjected to bias-extension and compression tests show that the proposed hinges preserve the characteristic second-gradient response of fibrous metamaterials while contributing to delay the onset of transverse instability (qualitative evidence). The improved compressive behavior suggests potential applications in lightweight fibrous composite metamaterials requiring enhanced stability and deformation control. A second-gradient continuum model is calibrated against the experimental bias-extension response and used to perform finite element based numerical simulations. The resulting simulations reproduce the experimental force–displacement behavior with very good accuracy, supporting both the effectiveness of the proposed hinge design and the relevance of the adopted higher-order continuum description.

Keywords. Pantographic metamaterials, Hinge mechanics, Additive manufacturing, Filament-based 3D printing, Second gradient theories.

Note. Article submitted by invitation.

Manuscript received 27 May 2026, revised and accepted 17 July 2026, online since 28 August 2026.

1. Introduction

Fibrous metamaterials [1–3] represent a distinct class within the larger category of mechanical metamaterials [4]. They are structurally characterized by assemblies of interconnected fibers whose mechanical interactions are mediated by specialized connecting mechanisms, typically

[*] Corresponding author

ISSN (electronic): 1873-7234 https://comptes-rendus.academie-sciences.fr/mecanique/

hinges. The mechanical behavior of these metamaterials is designed a priori to achieve specific deformation patterns or desired mechanical responses [5–11]. Among various fibrous metamaterials, pantographic structures stand out due to their distinctive mechanical properties and versatile applicability [12–16].

In the wide framework of fibrous metamaterials, the pantographic ones are defined by a particular internal microarchitecture [14] consisting of at least two families of parallel fibers arranged in a regular grid-like geometry. These fibers intersect at defined points where they are connected through some hinges, sometimes called *pivots* in the literature, allowing controlled rotation and deformation at these intersections. The hinges can vary based on the intended mechanical performance: they may either be ideal (perfectly frictionless and free to rotate without resistance) or elastic (providing some measurable flexibility through controlled deformation). This flexibility in hinge design enables significant yet stable deformation of the structure, making pantographic metamaterials exceptionally suitable for applications demanding efficient energy absorption, controlled vibration damping, and adaptive load management [17–20].

Due to their sophisticated and adaptable internal architecture, pantographic metamaterials may exhibit good capabilities in dissipating energy through controlled deformation. Consequently, they can be used to effectively dampen vibrations caused by seismic activities or dynamic loading conditions typical in bridge structures [21]. Acting as passive vibration isolation systems, these materials can notably reduce oscillation amplitudes, thus significantly enhancing the stability, reliability, and longevity of various civil engineering structures.

Beyond vibration reduction, pantographic metamaterials possess mechanical characteristics relevant to numerous fields, including Civil and Mechanical Engineering [22–24]. Additionally, these structures serve as valuable tools in validating and illustrating specific aspects of generalized Continuum Mechanics theories [25–31]. A notable feature of these materials is their capacity to undergo large elastic deformations without surpassing their elastic limit, ensuring structural integrity even under substantial mechanical loads [14,32]. Nevertheless, achieving optimal hinge configurations remains challenging, particularly regarding ease of fabrication and practical functionality [33,34].

In recent years, additive manufacturing has emerged as one of the most effective and versatile techniques for fabricating fibrous metamaterials [35–37]. Traditionally, perfect hinges have been successfully fabricated using selective laser sintering (SLS), even in metallic materials [38,39]. However, SLS-produced components often exhibit significant porosity at the microstructural level, making it challenging to describe these materials accurately using traditional continuous Cauchy mechanical models [39]. Moreover, the fabrication of miniature hinges through SLS is complicated by the tendency for internal hinge gaps to become obstructed by residual powder, resulting in increased friction and compromised performance [36,38,39].

To overcome these issues, a novel hinge design specifically optimized for filament-based 3D printing has been recently proposed in [40]. Filament printing technologies provide a cost-effective alternative to SLS, making the production of advanced metamaterials more accessible. Crucially, the newly developed hinge configuration contributes to delay the onset of transverse instability under compressive loading (qualitative evidence), which is a common issue in slender structures, although detailed analysis of buckling behavior is beyond the current scope. Conventional hinges used in pantographic systems typically involve cylindrical pins facilitating relative rotation between fibers [36]; the innovative hinge proposed in [40] enhances these traditional designs by ensuring precise, nearly frictionless rotations, thus substantially improving the mechanical reliability and performance of filament-printed pantographic metamaterials.

The (old) hinge concept shown in Figure 1 exhibits two main drawbacks. Firstly, when filament-based 3D printing is employed, its specific geometry is extremely difficult, if not impossible, to realize without support material; due to the small dimensions of the specimens,

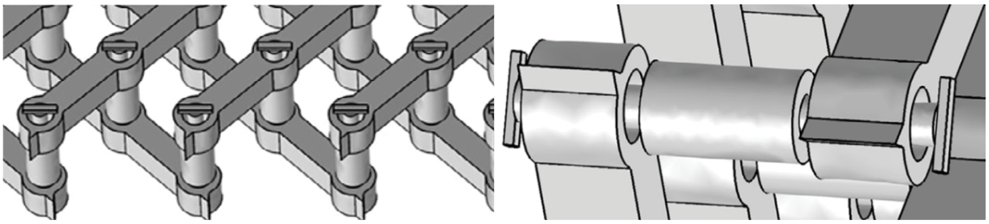

(a) Overall view. **(b)** Detail view.

Figure 1. Old conception of perfect hinges used in pantographic metamaterials [39]; reproduced for completeness.

supports tend to be melted to fibers and hinges, while soluble-support materials, dissolvable in water or solvents, are more expensive, slower to print and not compatible with all printers. Secondly, the hinges of Figure 1 do not mitigate the issue of transverse instability: their procumbent, horizontally disposed cross-section makes the structure prone to out-of-plane buckling under compressive loading.

The present work builds on these premises. The novel hinge design proposed in [40] is here investigated in greater detail through complementary bias-extension and compression tests on a PLA filament-printed specimen; the experimental campaign is then complemented by a second-gradient continuum model whose stiffness parameters are calibrated according to the same procedure adopted in [41] for lattice metamaterials, here specialized to the case of a single pantographic sheet equipped with perfect pivots. The paper is organized as follows. Section 2 reviews additive-manufacturing techniques for fibrous metamaterials and recalls the novel hinge design of [40]. Section 3 presents the experimental campaign, including both bias-extension and compression tests. Section 4 introduces the discrete-to-continuum second-gradient model and details the parameter-calibration procedure. Section 5 discusses the innovative aspects of the proposed hinges in the light of the experimental and numerical findings. Concluding remarks are gathered in Section 6.

The original contributions of the present work can be summarized as follows. First, it provides the first mechanical characterization of the hinge introduced in [40], which had previously been shown to be printable but was never tested under bias-extension and compression. Second, it gives the first quantitative confirmation of the near-frictionless character of that hinge, obtained a posteriori through the $K_s = 0$ calibration. Third, it specializes and simplifies the identification procedure of [41] to the case of a single pantographic sheet, reducing it to a two-step, decoupled calibration. It should be emphasized that the present study is intended as a proof-of-concept: it demonstrates that the hinge of [40] can be printed support-free as designed and that a single pantographic sheet so obtained exhibits the qualitative second-gradient behavior reproduced by the framework of [41]. Turning these qualitative findings into quantitative, statistically robust design data requires a dedicated campaign on multiple, independently tested specimens, which is identified here as the primary direction of future work.

2. An innovative hinge mechanism for pantographic metamaterials

2.1. *Additive manufacturing techniques for fibrous metamaterials*

Additive manufacturing has improved the fabrication of metamaterials by enabling the creation of complex micro-architectures with tailored mechanical properties. Among the various 3D printing techniques, Selective Laser Sintering (SLS), resin-based printing and filament-based

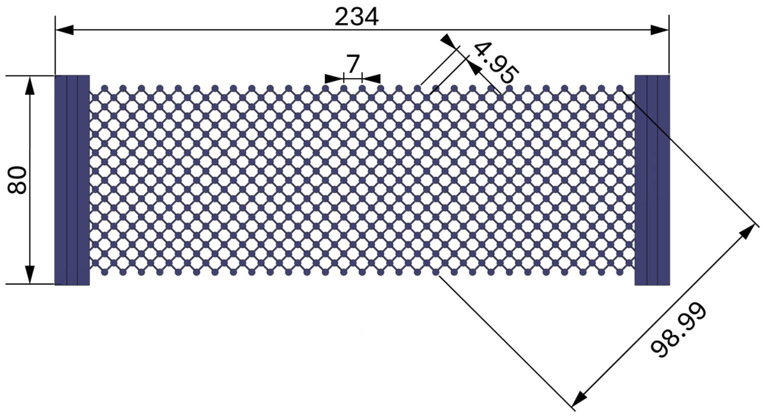

Figure 2. Geometry of the 3D-printed specimen. All dimensions are expressed in mm. Adapted from [40] for completeness.

printing are the most relevant ones. SLS facilitates the production of intricate geometries without the need for support structures, making it suitable for creating internal voids and complex lattice structures; it is however associated with high costs and potential thermal-shrinkage artifacts. Resin-based printing offers high precision but often results in brittle components requiring extensive post-processing. Filament-based printing is by far the most cost-effective, but can suffer from layer delamination and reduced geometric accuracy.

In the context of pantographic metamaterials the choice of additive-manufacturing technique is critical. Traditional hinge designs often incorporate right-angle overhangs, such as the heads of pins within the hinges. When filament-based printing is used, these overhangs lead to defects due to the phenomenon known as *bridging*, whereby unsupported filament strands sag or deform during printing. This results in lobed shapes that compromise hinge functionality. Incorporating support structures is challenging, as their removal can damage the delicate hinge components. For this reason it is very important to design a hinge which can be printed without any support still allowing for free rotations.

2.2. *Novel hinge conception*

A pantographic metamaterial is composed of interconnected unit cells arranged in a regular lattice structure [14], see Figure 2. Each unit cell consists of slender beams connected through specifically designed hinges, allowing significant deformation.

The precision and performance of pantographic metamaterials critically depend on the reliability of their printed hinges. The hinges constitute the functional core of these structures and determine their mechanical response and overall effectiveness. Precisely fabricated hinges allow controlled, smooth and predictable rotational movements at the fiber intersections, enabling the lattice to exhibit extensive, repeatable expansion, contraction and bending behaviors. High-quality hinges significantly reduce internal stresses and minimize unwanted resistance, ensuring that the metamaterial's deformation accurately aligns with its intended design.

The innovative hinge design illustrated in Figure 3a, introduced in [40], has been specifically optimized for filament-based 3D printing. The design eliminates significant overhangs and unsupported features, which are common obstacles encountered in filament printing and typically require additional support material. The carefully integrated rounded geometries and smooth transitional surfaces substantially reduce the occurrence of filament bridging, thus ensuring

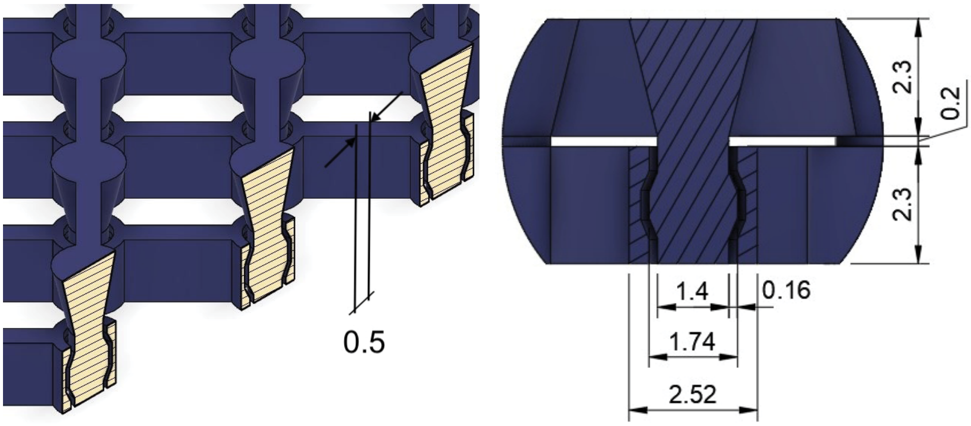

(a) New conception of perfect hinges, cross-section **(b)** Detail view.

Figure 3. Geometry of the new perfect hinge. All dimensions are expressed in mm. Adapted from [40] for completeness.

clean, dimensionally accurate hinges directly from the printing process and removing the need for complex post-processing. The hinge geometry includes interlocking contours and a vertical layer orientation deliberately chosen to align with the filament deposition path, thus maximizing printing efficiency and structural integrity. The alignment of the deposition direction with the longitudinal axis of the hinge enhances interlayer adhesion and significantly reduces the risk of delamination.

A specimen has been fabricated for the experimental campaign reported in Section 3, with the central objective of demonstrating that filament-based 3D printing can produce specimens whose mechanical performance closely matches that typically achieved with SLS [42,43]. Figure 2 reports the global dimensions of the manufactured specimen, while Figure 3b details the specific geometric parameters used in the innovative hinge design. Unlike the previous designs (Figure 1b), which rely on an internal cylindrical pin serving as the relative axis of rotation, the current hinge concept introduces a double-mechanism approach: the lower fiber incorporates a carefully engineered ring-shaped segment that accommodates a lobed pin securely attached to the upper fiber. This configuration is designed to reduce frictional forces by distributing the relative rotation over a contact region rather than concentrating it on a single cylindrical pin (the quantitative, macroscopic manifestation of this near-frictionless behavior being provided a posteriori by the reproduction of the bias-extension response with $K_s = 0$, Section 4), and it enhances the rotational smoothness of the hinge while minimizing the printing defects associated with bridging and unsupported features.

2.3. *Geometric and material characteristics of the specimen*

For the convenience of the reader, the geometric and material characteristics of the filament-printed specimen analyzed in this work are summarized in Table 1. The data are organized in three groups: the overall geometry of the pantographic sheet (Figure 2), the geometry of the individual hinge (Figure 3b), and the elastic properties of the printed material.

The specimen has overall dimensions of 234×80 mm^2, with two clamping strips of width 7 mm at the two short ends. The aspect ratio of approximately 3:1 between the long and the short side is fully consistent with the conventional $L = 3\ell$ choice adopted in Section 4.1 for the continuum description of the bias-extension test. The two families of parallel fibers are arranged at ±45° with

Table 1. Geometric and material characteristics of the filament-printed pantographic specimen analyzed in this work

Quantity	Symbol	Value
Specimen geometry (Figure 2)		
Overall length	L	234 mm
Overall width	ℓ	80 mm
Aspect ratio	L/ℓ	≃3
Clamping-strip width	w_c	7 mm
Inter-hinge distance along a fiber	p	4.95 mm
Fiber orientation w.r.t. the long axis	θ_0	±45°
Hinge geometry (Figure 3b)		
Internal gap	g	0.16 mm
Overall transverse dimension of the hinge	d_h	2.52 mm
Depth of the rotating part	ℓ_h	1.4 mm
Vertical thickness of the fiber at the hinge	h_f	2.3 mm
In-plane thickness of the fiber	t_f	0.5 mm
Diameter of the lobe	d_ℓ	1.74 mm
Material—SUNLU PLA filament		
Young's modulus	E	3500 MPa
Flexural modulus	E_{flex}	2240 MPa
Poisson's ratio (assumed)	ν	0.33 ÷ 0.35

respect to the long axis of the specimen, which is the direction along which the displacement is prescribed during the bias-extension test [44]. The inter-hinge distance along a fiber, which plays the role of the parameter p in the de Saint Venant estimates of Section 4.2, equals $p = 4.95$ mm.

Regarding the hinge geometry, the most critical feature is the internal gap of 0.16 mm between the ring-shaped segment on the lower fiber and the lobed pin on the upper fiber: this is the parameter that controls the relative rotation of the two interconnected fibers and, ultimately, the near-frictionless character of the pivot. This value was not optimized against friction; it was chosen as the minimum clearance that, given the resolution of the filament printer (nozzle diameter 0.2 mm and layer height 0.08 mm), reliably yields an open, non-fused gap in a single, support-free print. Qualitatively, a larger gap increases the play/backlash and the risk of fiber misalignment, whereas a smaller gap increases the risk of fusion and of residual contact friction, so that the adopted value represents a manufacturability-driven compromise between these two effects; a systematic optimization of the gap is left to future work. The overall transverse dimension of the hinge is 2.52 mm, while its main internal feature has a depth of 1.4 mm. The vertical thickness of the upper and lower portions of the hinge are both equal to 2.3 mm, separated by the internal gap.

The specimen has been produced from a SUNLU PLA filament. The Young's modulus declared on the Technical Data Sheet is $E = 3500$ MPa and the flexural modulus is $E_{\text{flex}} = 2240$ MPa; the Poisson's ratio is not provided by the manufacturer and is assumed in the range $\nu = 0.33 \div 0.35$, which is typical for filament-printed PLA [40]. These values are used in the de Saint Venant initial estimate of the stiffness parameters of the continuum model (Section 4.2) and as the material reference for the calibration procedure described in Section 4.3. It should be recalled that the actual effective stiffness of the printed material is known to be reduced and slightly anisotropic with respect to these nominal values, due to the layered nature of the filament-deposition

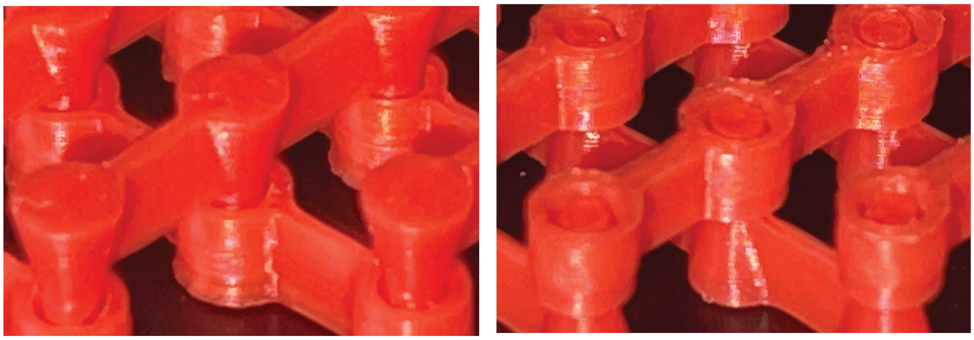

(a) Top view. **(b)** Bottom view.

Figure 4. Detail of 3D-printed hinges.

process; this aspect motivates the use of Table 1 as a geometric and material reference rather than as a definitive set of effective elastic constants for the homogenized lattice.

3. Experimental campaign

The experimental tests have been performed on the specimen described in Sections 2.2 and 2.3, whose geometric and material characteristics are summarized in Table 1.

Details of the printed hinges are shown in Figure 4 for the top view (a) and the bottom view (b). As can be observed from Figure 4b, the internal gap of 0.16 mm has been correctly fabricated, and free relative rotations between the fibers are allowed.

Two complementary tests have been carried out on the same specimen, namely a bias-extension test (Section 3.1) and, successively, a compression test (Section 3.2). The bias-extension test is so called because the direction of the prescribed displacement is *biased* with respect to the directions of the two fiber families [44]. It is worth pointing out from the outset that the two tests have been performed sequentially on the same physical specimen, with the bias-extension test preceding the compression test; this aspect will be reconsidered when discussing the numerical comparison in Section 4.4.

3.1. *Bias-extension test*

The force–displacement curve recorded during the bias-extension test is shown in Figure 5. The response is qualitatively very similar to that observed in SLS-produced specimens [42,43], with a well-defined initial regime followed by a strongly nonlinear stiffening branch.

In the initial regime, the deformation is essentially accommodated by the bending of the fibers in the transition zones between the clamped triangular regions and the central free zone, while the central part of the specimen undergoes a nearly rigid pantographic motion. As the prescribed displacement increases, the fibers in the central zone progressively come into mutual contact and the dominant deformation mechanism shifts towards axial stretching of the fibers, which produces the characteristic exponential-like stiffening of the curve. This transition from a bending-dominated to a stretching-dominated regime is precisely the mechanism that, in the continuum description, marks the passage from a second-gradient to a first-gradient response, and which makes pantographic structures interesting candidates as "mechanical diodes" [42,43].

The deformation pattern depicted in Figure 6 corroborates the previous reading. Near the clamped boundaries, two triangular zones remain essentially rigid; at the interface between these

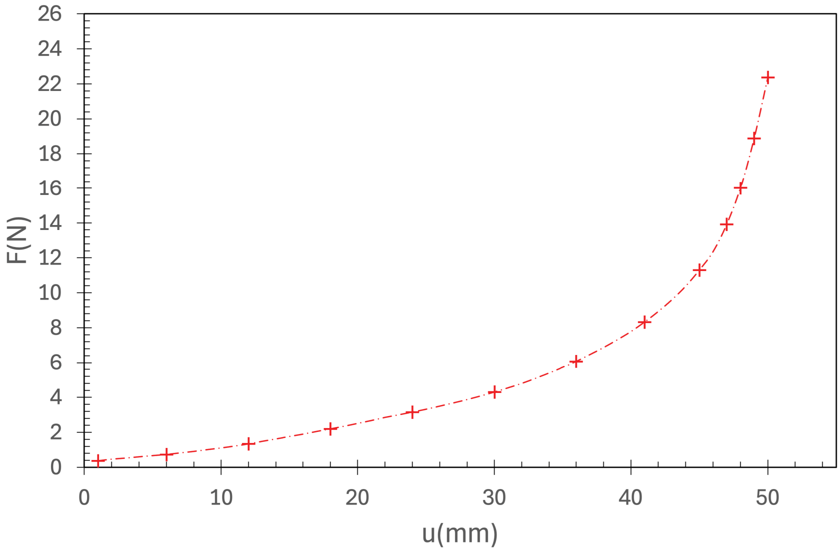

Figure 5. Bias-extension test: measured reaction force versus prescribed displacement.

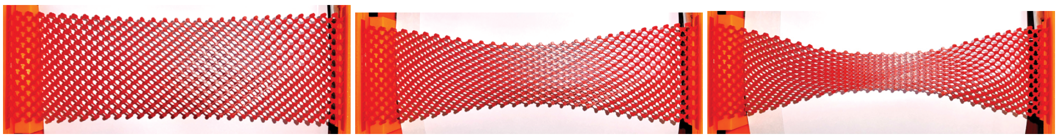

(a) (b) (c)

Figure 6. Deformed shape of the specimen during the bias-extension test at three increasing prescribed displacement steps: (a) intermediate stage, (b) advanced stage, (c) final stage.

zones and the central area, the fibers exhibit a clear bending. In the central area, conversely, the fibers undergo almost pure relative rotations, with little appreciable bending, which is the kinematic signature of an ideal pantographic response. The clean separation between bending- and rotation-dominated regions is a direct consequence of the near-frictionless behavior of the new hinges: any non-negligible torsional resistance at the pivots would smear this separation and obscure the second-gradient signature of the lattice [14].

3.2. *Compression test*

A compression test was performed on the same specimen, in order to assess the influence of the new hinge design on the response of the lattice in the regime where the conventional hinge concept of Figure 1 is known to be most problematic. As recalled in the Introduction, the procumbent cross-section of the conventional design promotes transverse instability under compressive loading; the new hinge, with its predominantly vertical layout and the absence of protruding pin heads, is expected to mitigate this issue.

The measured force–displacement curve is reported in Figure 7. The response is markedly softer than its tensile counterpart, in agreement with the intrinsically asymmetric behavior of pantographic lattices [45]. In the early stages of loading the curve is essentially linear and is governed by the bending of the fibers (in fact, no torsional energy of hinges is included because

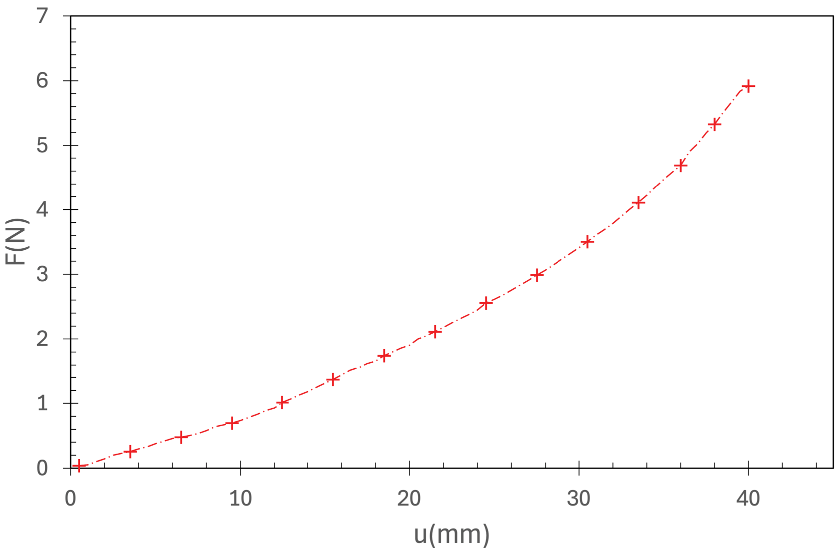

Figure 7. Compression test: measured reaction force versus prescribed displacement.

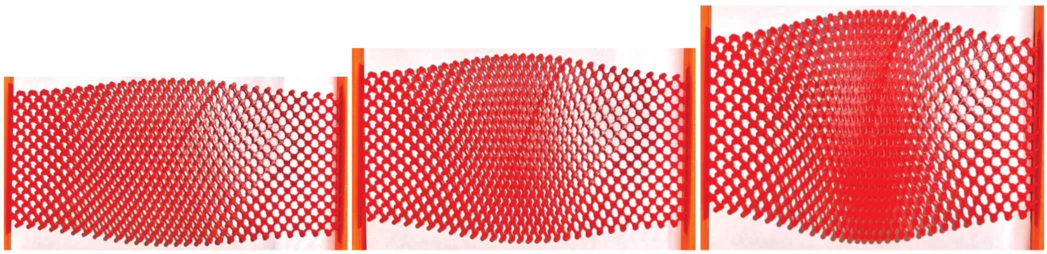

(a) (b) (c)

Figure 8. Deformed shape of the specimen during the compression test at three increasing prescribed displacement steps: (a) intermediate stage, (b) advanced stage, (c) final stage.

these are perfect; in case of elastic or elasto-plastic hinges, their torsion would influence this first-stage behavior); as the displacement increases, the central zone develops a "pillow"-shaped deformation (Figure 8) typical of compressed pantographic lattices. Crucially, no abrupt drop in the reaction force is observed within the explored displacement range, indicating that the new hinge design effectively postpones the onset of macroscopic out-of-plane instability with respect to specimens equipped with the conventional hinge design [39] (qualitative evidence; a quantitative buckling analysis is left to a dedicated future investigation).

3.3. *Combined tension–compression response*

The two branches obtained from the bias-extension and compression tests can be assembled into a single force–displacement diagram (Figure 9), in which the prescribed displacement is taken as the signed elongation of the specimen along the bias direction. The resulting curve clearly highlights the marked asymmetry between the tensile and compressive regimes, which is the defining feature of pantographic metamaterials and the rationale behind their interpretation as mechanical diodes [42,43].

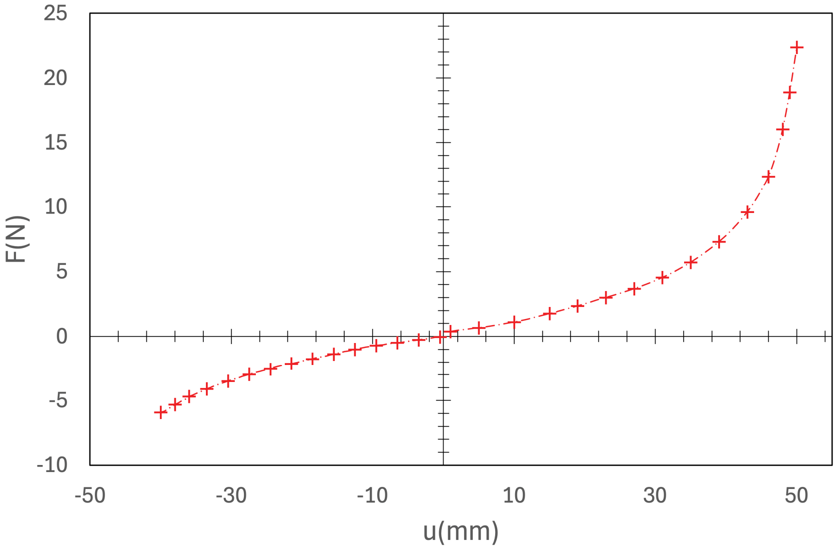

Figure 9. Combined tension–compression response: measured reaction force versus prescribed displacement.

4. Second-gradient continuum model and parameter calibration

In this section, the experimental campaign is complemented by a continuum model of the pantographic specimen. We follow the framework recently established in [41], but tailored to the present setting in two respects. First, the specimen is a single pantographic sheet, so the mesoshear deformation mechanism between adjacent fiber layers (and the corresponding interlayer stiffness K_{int} introduced in [41]) does not apply here. Second, and most importantly, the hinges of the present design have been shown in Section 3.1 to behave as perfect pivots, with a clean separation between bending- and rotation-dominated regions in the deformation pattern of Figure 6; this observation justifies the modeling assumption $K_s = 0$ (where K_s denotes the hinge stiffness penalizing the change of the angle between the two fiber families at each pivot, see Equation (2)) adopted throughout this section, so that the torsional energy of the hinges vanishes identically and only the fiber elongation stiffness K_e and the fiber bending stiffness K_b remain to be calibrated.

4.1. *Continuum model*

The homogenized description of the pantographic sheet involves three lumped stiffnesses: the fiber elongation stiffness K_e, penalizing the axial deformation of the fibers (a first-gradient contribution); the fiber bending stiffness K_b, penalizing their curvature (a second-gradient contribution); and the hinge stiffness K_s, penalizing the relative rotation of the two fiber families at each pivot. In the present work K_s is set to zero (Equation (3)), so that only K_e and K_b are calibrated.

Following [14,41], the specimen is described as a two-dimensional continuum whose reference shape is the rectangular domain $\Omega = [0, L] \times [0, \ell] \subset \mathbb{R}^2$, with $L = 3\ell$ as customary for the bias-extension test [32,44]. The current shape of the specimen is represented through a placement field $\boldsymbol{\chi} : \Omega \to \mathbb{R}^2$, assumed at least twice continuously differentiable. We denote by $\boldsymbol{F} = \nabla\boldsymbol{\chi}$ the deformation gradient and we introduce an orthogonal pair of unit vectors $(\boldsymbol{D}_1, \boldsymbol{D}_2)$ aligned, in the reference configuration, with the two fiber families.

Asymptotic homogenization of the underlying discrete pantographic microstructure [14,32] produces a macroscopic strain energy that contains a first-gradient (fiber elongation) and a second-gradient (fiber bending) contribution. This part of the strain energy, denoted $\mathscr{U}_f$ (the fiber strain energy, collecting the axial first-gradient and the bending second-gradient contributions of the two fiber families), reads:

$$\mathscr{U}_f(\boldsymbol{\chi}) = \int_\Omega \sum_{\alpha=1}^{2} \frac{K_\mathrm{e}}{2}(\|\boldsymbol{F}\boldsymbol{D}_\alpha\| - 1)^2 \,\mathrm{d}\Omega + \int_\Omega \sum_{\alpha=1}^{2} \frac{K_\mathrm{b}}{2}\left[\frac{(\nabla\boldsymbol{F}\,|\,\boldsymbol{D}_\alpha\otimes\boldsymbol{D}_\alpha)\cdot(\nabla\boldsymbol{F}\,|\,\boldsymbol{D}_\alpha\otimes\boldsymbol{D}_\alpha)}{\|\boldsymbol{F}\boldsymbol{D}_\alpha\|^2} - \left(\frac{\boldsymbol{F}\boldsymbol{D}_\alpha}{\|\boldsymbol{F}\boldsymbol{D}_\alpha\|}\cdot\frac{\nabla\boldsymbol{F}\,|\,\boldsymbol{D}_\alpha\otimes\boldsymbol{D}_\alpha}{\|\boldsymbol{F}\boldsymbol{D}_\alpha\|}\right)^2\right]\mathrm{d}\Omega, \quad (1)$$

where $(\nabla\boldsymbol{F}\,|\,\boldsymbol{D}_\alpha\otimes\boldsymbol{D}_\alpha)^\beta = F^\beta_{\alpha,\alpha} = \chi^\beta_{,\alpha\alpha}$ and Greek indices run over $\{1,2\}$. The first integral represents the energy stored in the axial deformation of the fibers, the second integral represents the energy stored in their bending and is, intrinsically, a second-gradient contribution.

In the general framework of [41], an additional energetic term accounting for the elastic torsion of the pivots is added to Equation (1):

$$\mathscr{U}_\mathrm{s}(\boldsymbol{\chi}) = \int_\Omega \frac{K_\mathrm{s}}{2}\left|\arccos\left(\frac{\boldsymbol{F}\boldsymbol{D}_1}{\|\boldsymbol{F}\boldsymbol{D}_1\|}\cdot\frac{\boldsymbol{F}\boldsymbol{D}_2}{\|\boldsymbol{F}\boldsymbol{D}_2\|}\right) - \frac{\pi}{2}\right|^\beta \mathrm{d}\Omega. \quad (2)$$

This term collects the elastic resistance to the change of the angle between the two fiber families at each hinge and is essential for the description of SLS-printed pantographic specimens, in which the residual powder lodged in the internal gap of the pivots introduces a non-negligible torsional stiffness [39,41]. In the present case, conversely, the experimental evidence collected in Section 3.1 indicates that the proposed hinges behave as near-perfect pivots: in particular, the clean kinematic separation between bending- and rotation-dominated regions in Figure 6 is incompatible with a sizable K_s [14]. We therefore set:

$$K_\mathrm{s} = 0, \quad (3)$$

so that $\mathscr{U}_\mathrm{s}$ vanishes identically and the total strain energy of the pantographic sheet reduces to:

$$\mathscr{U}(\boldsymbol{\chi}) = \mathscr{U}_f(\boldsymbol{\chi}), \quad (4)$$

which depends on the two stiffness parameters K_e and K_b only. The exponent β appearing in Equation (2) becomes irrelevant under the assumption in Equation (3) and is therefore not discussed further.

4.2. *Initial estimate of the stiffness parameters via de Saint Venant beam theory*

A first estimate of the stiffness parameters K_e and K_b is obtained from the material constants of the printed fibers and from the geometry of the unit cell, following the de Saint Venant beam approach already used in [14,28,41,46]. The two retained lumped stiffnesses are related to the geometric and material parameters of the specimen as [41]:

$$K_\mathrm{e} = \frac{EA}{p}, \quad K_\mathrm{b} = \frac{EJ}{p}, \quad (5)$$

where E is Young's modulus of the printed material, A and J the area and moment of inertia of the fiber cross-section, and p the distance between adjacent hinges along a fiber. Each of these geometric quantities is read off from Figures 2 and 3b. The Young's modulus is taken equal to the nominal value of the PLA filament, $E = 3500$ MPa. The third relation reported in [41] for the hinge torsion stiffness, $K_\mathrm{s} = G\pi r^4/(2hp^2)$, does not enter the present calibration because of the assumption in Equation (3).

As remarked in [41], the values obtained through Equation (5) are not yet optimal for 3D-printed samples and must be subsequently scaled to account for the layered, non-fully-continuous nature of the printed material. In the present case, the effect of the filament-deposition process on the actual stiffness of the fibers is further amplified by the different printing technology adopted (filament versus SLS) and by the fact that filament-printed PLA exhibits a marked anisotropy linked to the layer orientation. The values obtained from Equation (5) are therefore used as initial guesses only, and are then refined as described next.

4.3. *Calibration procedure and final values*

The calibration of the two stiffness parameters K_e and K_b is performed following the procedure introduced in [41], which exploits the natural separation of the deformation regimes typical of a pantographic sheet under bias extension. Each parameter is associated, in a clearly identifiable portion of the experimental force–displacement curve, with a dominant deformation mechanism; this allows one to perform the calibration in a sequential, almost decoupled fashion, rather than as a global nonlinear fit. The further simplification with respect to [41], made possible by the perfect-pivot assumption of Equation (3), is that the intermediate stage of the calibration (devoted in [41] to the identification of K_s and of the exponent β) is no longer needed, and the procedure reduces to two steps only.

The bending stiffness K_b is a property of the homogenized model. It can be identified by adjusting it so that the numerical force–displacement curve correctly reproduces the curvature of the initial branch of the experimental curve, where bending of the fibers in the transition zones is the dominant deformation mechanism (Figures 5 and 6). This stage of the calibration is consistent with the observations of [44,47,48] on the role of the bending stiffness in the early bias-extension response of pantographic sheets.

The elongation stiffness K_e governs the axial deformation of the fibers and is dominant in the late stages of the bias-extension curve of Figure 5, where the fibers in the central zone come into mutual contact and stretching becomes the leading deformation mechanism. As suggested in [41], K_e could in principle also be determined through an independent tensile test on a single printed fiber; in the present work it is identified by adjusting it so that the numerical curve reproduces correctly the steep, exponential-like force increase observed in the high-displacement branch of the experimental data.

The result of the procedure outlined above leads to the following calibrated stiffness parameters for the present filament-printed specimen:

$$K_e = 7.4246 \times 10^5 \text{ N/m}, \quad K_b = 8.3527 \times 10^{-2} \text{ N·m}, \quad K_s = 0. \tag{6}$$

As anticipated in Section 4.2, both calibrated stiffnesses are reduced with respect to the de Saint Venant initial estimates of Equation (5); this is the same trend observed in [41] for the elongation stiffness, and is here further accentuated by the marked anisotropy of the filament-printed PLA along the layer-deposition direction. No torsional contribution is needed in order to reproduce the experimental curve, as discussed in detail in the next subsection.

As discussed in [41], calibrating the stiffness parameters from a single force–displacement curve is a deliberate simplification: a more comprehensive identification could exploit additional experimental quantities such as fiber angles, fiber elongations and central striction. In the present case, the calibration is restricted to the bias-extension force–displacement curve, while the compression branch of Figure 7 is left out of the fit and used a posteriori to assess the limits of the elastic model under reversed loading.

4.4. *Numerical simulations and comparison with experimental data*

The finite element implementation of the strain energy in Equation (4) is performed using Lagrange quadratic shape functions and a Newton-based iterative solver, in line with the numerical

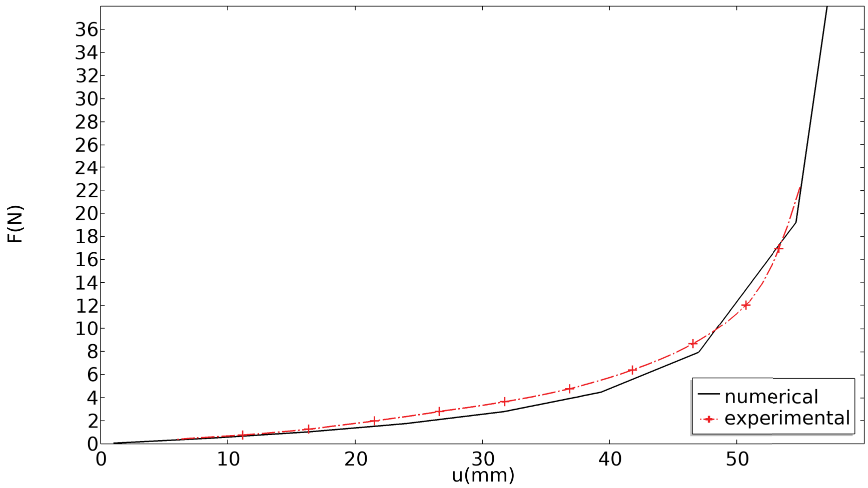

Figure 10. Comparison between the numerical force–displacement curve obtained with the calibrated second-gradient model (black solid line) and the experimental data of the bias-extension test (red dash-dotted line with markers).

framework adopted in [41]. The simulations reproduce the geometry of the printed specimen (Figures 2 and 3b) and the boundary conditions of the experimental tests of Section 3, using the calibrated stiffness parameters of Equation (6).

The numerical force–displacement curve obtained for the bias-extension test is reported in Figure 10 together with the experimental data of Section 3.1. The agreement is remarkable along the whole loading range: the calibrated model captures both the soft initial branch, dominated by fiber bending, and the steep nonlinear stiffening associated with fiber stretching at large displacements. The fact that this match is obtained with $K_s = 0$, i.e. without any torsional contribution from the pivots, provides a direct quantitative confirmation that the proposed hinges behave as near-perfect pivots: any non-negligible K_s would have produced an elastic offset in the initial branch of the numerical curve, which is not observed in the experimental data.

We want to remark the role of the torsional stiffness K_s. A non-zero K_s adds a torsional energy term (see Equation (2)) that penalizes the relative rotation of the two fiber families; its main effect is to stiffen the initial, rotation-dominated branch of the response, since the central region, which in the ideal case undergoes an almost pure pantographic rotation, would then oppose an elastic resistance. The result is an offset in the low-displacement part of the force–displacement curve and a progressive smearing of the clean separation between bending- and rotation-dominated regions observed in Figure 6. This is illustrated in Figure 11, which compares the bias-extension curve computed for $K_s = 0$ with those obtained for two non-zero values of K_s: the initial branch is progressively lifted as K_s increases, whereas the experimental data are compatible only with $K_s \approx 0$. A direct measurement of the pivot friction would provide even more direct evidence and is left to future work. Interesting results of this kind have already been obtained in [49,50].

The spatial distribution of the deformation field predicted by the calibrated model is reported in Figure 12 for the bias-extension test and in Figure 13 for the compression test, at three increasing prescribed displacement steps in each case. The color map represents the local value of the strain energy density, superimposed on the deformed configuration of the specimen; the original undeformed rectangular contour is drawn in black for reference. Three features are common to all six maps and constitute, together, the spatial signature of an ideal pantographic kinematics. First, two low-intensity dark zones appear at the clamped ends of the specimen,

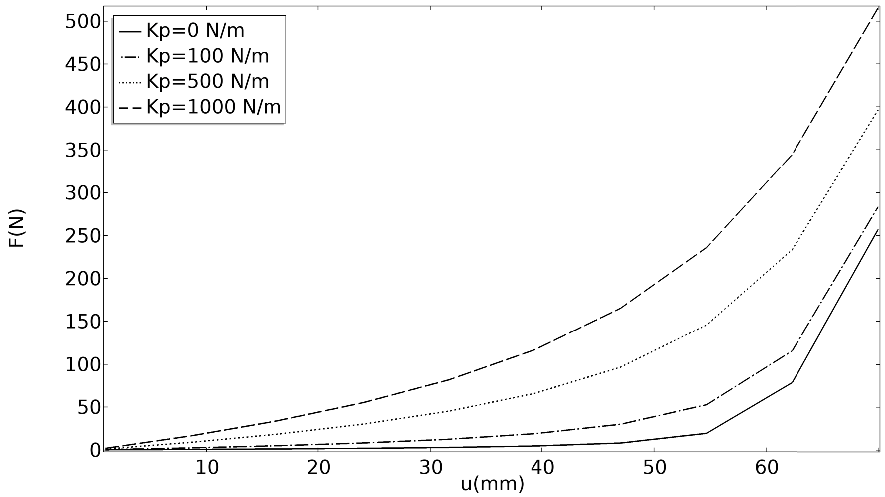

Figure 11. Effect of a non-zero hinge stiffness K_S on the numerical bias-extension response: the initial, rotation-dominated branch is progressively lifted as K_S increases, whereas the experimental data are compatible only with $K_S \approx 0$. (New figure.)

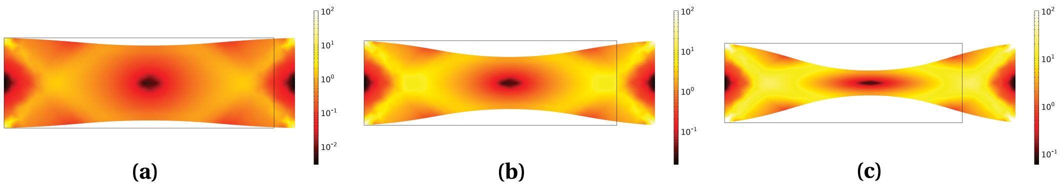

(a) **(b)** **(c)**

Figure 12. Numerical deformation pattern predicted by the calibrated second-gradient model for the bias-extension test, at three increasing prescribed displacement steps: (a) intermediate stage, (b) advanced stage, (c) final stage. The color map shows the local value of the strain energy density expressed in N/m; the undeformed rectangular contour of the specimen is drawn in black for reference.

in correspondence with the rigid triangular regions identified experimentally in Section 3. Second, a characteristic “X”-shaped pattern of higher-intensity bands emanates from the clamped corners and converges toward the centerline of the specimen; these bands mark the transition zones between the rigid triangles and the central pantographic region, where the fibers undergo their most pronounced bending. Third, a dark, low-intensity ellipse appears at the geometric center of the specimen, signaling that the central region undergoes an almost pure pantographic rotation with negligible bending or stretching of the fibers. The only qualitative difference between extension and compression lies in the outer contour of the deformed specimen, which contracts laterally in the bias-extension test (necked shape, Figure 12) and bulges laterally in the compression test (pillow shape, Figure 13). The progression across the three displacement steps in each figure shows how the X-shaped bands become progressively more pronounced and how the spatial extent of the central low-deformation ellipse evolves, in full agreement with the experimental deformation snapshots of Figures 6 and 8.

4.4.1. *Force–displacement response in compression*

The numerical force–displacement curve obtained for the compression test, computed with the very same calibrated parameters of Equation (6), is reported in Figure 14 together with the experimental data of Section 3.2. Since these parameters were identified in a decoupled

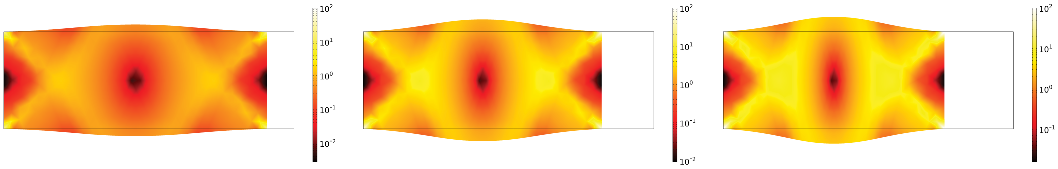

(a) (b) (c)

Figure 13. Numerical deformation pattern predicted by the calibrated second-gradient model for the compression test, at three increasing prescribed displacement steps: (a) intermediate stage, (b) advanced stage, (c) final stage. Color map and reference contour as in Figure 12.

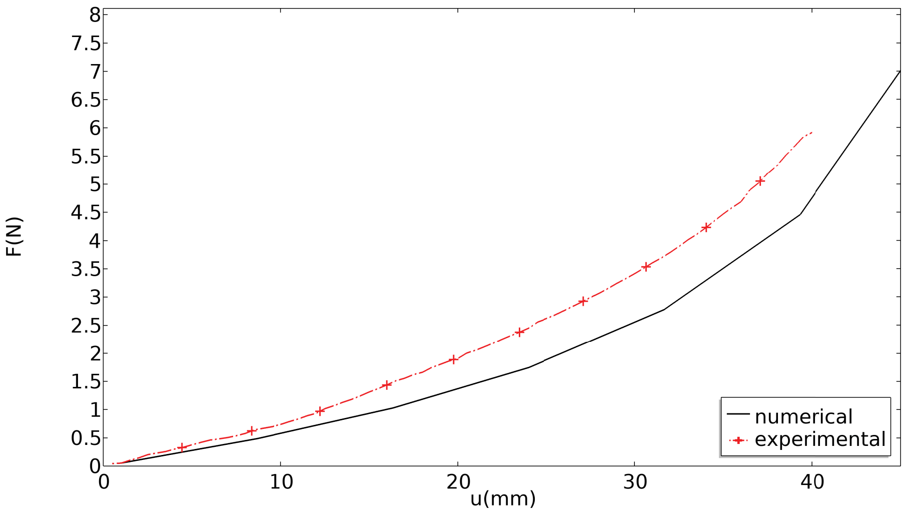

Figure 14. Comparison between the numerical force–displacement curve obtained with the calibrated second-gradient model (black solid line) and the experimental data of the compression test (red dash-dotted line with markers).

fashion from the bias-extension test alone (K_b from the initial bending-dominated branch and K_e from the late stretching-dominated branch) and the compression branch was not used in the calibration, this comparison constitutes an independent, out-of-sample prediction rather than a second fit. The agreement is qualitatively good, with the two curves sharing the same shape and the same final stiffening behavior. Quantitatively, however, a systematic offset is observed: the experimental reaction force is consistently slightly larger in absolute value than the one predicted by the model along the whole compressive branch, and the two curves remain roughly parallel up to the maximum prescribed displacement.

In fact, as already pointed out in Section 3, the bias-extension and the compression tests have been performed sequentially on the same physical specimen, with the compression test following the bias-extension one. During the bias-extension test, the fibers located in the transition zones underwent a non-negligible bending in a well-defined direction (Figure 6); when the same specimen is subsequently loaded in compression, those same fibers are forced to bend in the opposite direction (Figure 8). In a perfectly elastic and isotropic fiber, the response in the two directions would coincide; in the present filament-printed PLA specimen, however, a slight residual stiffening of the previously bent fibers, when reloaded in the opposite direction, is a plausible mechanism. Layer-by-layer filament deposition is known to introduce a marked anisotropy in the printed material, and prior-loading-induced reorientation of the polymer chains can result in a mildly direction-dependent flexural response. Under this interpretation, the experimental compression curve would slightly overestimate the compressive response of the specimen, and the offset visible in Figure 14 would be a measure of this preconditioning rather than a limitation of the calibrated model. This is admittedly only a working hypothesis at this stage; its validation (or revision) requires a dedicated experimental campaign of cyclic tension–compression tests, possibly on multiple specimens with controlled loading histories, in which the dependence of the compressive response on the prior bending direction of the fibers can be quantified. Such a campaign is left to a future investigation.

5. Discussion

The combined experimental and numerical evidence collected in Sections 3 and 4 can now be used to summarize the distinctive features of the hinge design introduced in [40] and to highlight in what sense it constitutes a genuine improvement over conventional pantographic pivots.

5.1. *Tailored geometry to filament-deposition process and mitigation of instabilities*

The most evident geometric novelty of the proposed hinge, with respect to the conventional design of Figure 1, is the suppression of the internal cylindrical pin and its replacement by a double-mechanism architecture made of a ring-shaped segment on the lower fiber that hosts a lobed counterpart attached to the upper fiber [40]. From the manufacturability standpoint, this choice eliminates the right-angle overhang associated with the head of the pin, which in conventional designs is the main source of bridging defects when filament-based 3D printing is employed [40]. From the mechanical point of view, the double-mechanism conception distributes the relative rotation over a contact region rather than concentrating it on a single cylindrical pin, which tends to reduce the local stress peaks at the pivot and to improve the smoothness of the rotation.

A second innovative aspect concerns the geometry of the hinge as a whole, which is intentionally designed to be compatible with the filament-deposition path [40]. The rounded shapes and gradual transitions minimize the local angles at which the filament must bridge unsupported regions, while the interlocking contours and the vertical layer orientation align the deposition direction with the longitudinal axis of the hinge. This alignment has two beneficial consequences: it maximizes the inter-layer adhesion in the most stressed parts of the hinge, thus reducing the risk of delamination, and it removes the need for soluble support material, which would otherwise be required for a clean print of the internal gap and which is incompatible with most low-cost, single-extruder filament printers. The combined effect is a hinge that can be reliably printed in a single, support-free operation while preserving the geometric features (in particular, the internal gap) that govern its mechanical behavior.

The detail views of the printed hinges reported in Figure 4 show that the nominal internal gap of 0.16 mm has been printed open and free of fused or support material, so as to allow free relative rotation of the two interconnected fibers; being global views, they are not intended to certify a metrological accuracy of the gap. This is a non-trivial result: in SLS-produced miniaturized hinges, the internal gap is frequently contaminated by residual powder that is extremely difficult to remove and that introduces a non-negligible friction at the pivot [39]. In contrast, the filament-deposition process, when applied to a geometry such as the present one that does not require support material in the gap region, produces a clean, dust-free gap directly at the end of the print, without any post-processing. The quantitative counterpart of this qualitative observation is provided in Section 4: the experimental bias-extension curve is faithfully reproduced by the model under the assumption $K_s = 0$, i.e. without invoking any torsional resistance at the pivot. This is the most direct quantitative manifestation of the near-frictionless character of the proposed hinges, in stark contrast with the non-negligible K_s values required for SLS-produced pantographic specimens [39,41].

A further benefit of the new hinge design, already anticipated in [40] and confirmed in the present work, concerns the response of the specimen under compressive loading. Conventional pantographic hinges (Figure 1) feature a procumbent, horizontally disposed cross-section of the fibers, which is mechanically efficient under axial extension but extremely unfavorable under compression, since it promotes out-of-plane buckling of the lattice. The new hinge, with its predominantly vertical layout and the suppression of the protruding pin heads, leaves the fibers with a much more favorable orientation of the principal axes of inertia with respect to the out-of-plane direction. The experimental evidence reported in Section 3.2 is fully consistent with this picture at a qualitative level: within the displacement range explored in the compression test, the force–displacement curve of Figure 7 does not exhibit any abrupt drop, and the deformation patterns of Figure 8 remain essentially in-plane until the very last step. A detailed quantitative analysis of the buckling load and of the post-buckling behavior is beyond the scope of the present work and is left to a dedicated future investigation.

Finally, it is worth recalling that the manufacturing technology employed in this work, namely filament-based fused deposition modeling, has a cost which is one to two orders of magnitude smaller than that of SLS, and is by now widely available in academic and industrial laboratories. The fact that the proposed hinge design can be reliably printed with such an accessible technology, and that its mechanical response is quantitatively comparable with that of SLS-produced pantographic specimens [42,43], is in itself a non-negligible practical innovation: it makes pantographic metamaterials genuinely available to a much larger community of researchers and practitioners.

5.2. *Hinges and matrix: a parallel with fiber-reinforced composites*

The analysis of Section 5 has emphasized to what extent the macroscopic response of a pantographic lattice is controlled by the character of its hinges. A nearly ideal hinge (frictionless and free to rotate) lets the pantographic kinematics emerge, while any deviation from this ideal condition (residual friction, elastic stiffness, geometric imperfection) contaminates the response with first-gradient contributions that progressively obscure the underlying second-gradient behavior. It is interesting to interpret this observation from the perspective of a class of composite materials in which no discrete pivots are present at all, but their role of kinematic constraints is played by a softer matrix surrounding the fibers.

Consider a two-phase composite consisting of an isotropic compliant matrix in which two interpenetrated families of parallel cylindrical fibers are embedded, the two families being alternately oriented at angles $\pm\theta$ with respect to a reference axis [51]. In the undeformed configuration the two families are mutually orthogonal, exactly as in a pantographic sheet, and under in-plane extension along the bisector of the two families the misorientation angle θ progressively decreases, in close analogy with what is observed in the central zone of a pantographic specimen during a bias-extension test (Figure 6). In such a composite, no discrete pivots are introduced between the fibers: the kinematic constraints that in a pantographic lattice are enforced by the hinges are here transmitted by the surrounding matrix, which acts as a *distributed kinematic mediator*. The matrix plays, in a continuous and compliant manner, the same role that the hinges play in a discrete fashion in the pantographic lattice.

The torsional stiffness K_s introduced in Equation (2) and set to zero in the present work quantifies, in the lattice description, the elastic resistance of the hinge to a change of the angle between the two fiber families; its direct counterpart in the composite description is the effective in-plane shear stiffness of the matrix. A softer matrix allows the fibers to rotate more freely with respect to each other and mimics a near-ideal pivot, whereas a stiffer matrix progressively suppresses the pantographic kinematics and mimics a torsionally stiff hinge. The limit of a perfect hinge, $K_s = 0$ (adopted as a modeling assumption in Section 4.1 and confirmed a posteriori by the agreement of the model with the bias-extension data), corresponds in the composite description to a vanishingly compliant matrix that imposes no resistance to the relative rotation of the two families; the opposite limit of a fully rigid hinge corresponds, in turn, to a matrix so stiff that it locks the fiber rotation altogether. The present filament-printed hinge is thus the lattice-level counterpart of the soft-matrix limit of the composite description: in both settings, the pantographic constraint between the two fiber families is enforced with the least possible mechanical contamination, and the same characteristic asymmetry between bending- and stretching-dominated regimes emerges.

The two viewpoints (discrete hinges and distributed matrix) should therefore be regarded as complementary routes toward the same kinematic target rather than as competing alternatives. The hinge design proposed in [40] and characterized in the present work realizes the pantographic constraint through a discrete, near-frictionless mechanism, while the composite description realizes it through a continuous, compliant matrix; both routes converge to the same macroscopic signature, namely the strong asymmetry between bending- and stretching-dominated regimes and the geometric saturation associated with the maximum admissible extension. This convergence reinforces the interpretation of pantographic kinematics as a structural paradigm whose macroscopic manifestation is largely insensitive to the specific microscopic mechanism through which the underlying constraint between the two fiber families is enforced, and it suggests that future hinge designs and future matrix-embedded pantographic composites should be developed in parallel rather than in isolation.

6. Conclusions

A novel hinge concept for pantographic metamaterials, recently introduced in [40] and specifically tailored to filament-based 3D printing, has been investigated through a combined experimental and numerical campaign. Bias-extension and compression tests have been performed on a PLA filament-printed specimen, and the experimental data have been complemented by a second-gradient continuum model whose stiffness parameters have been calibrated according to the procedure recently established for lattice metamaterials in [41]. No interlayer mesoshear contribution and no hinge torsion contribution are required: a single placement field is sufficient to describe the deformation, and the modeling assumption $K_s = 0$ reduces the calibration to two stiffness parameters only, namely K_e and K_b.

The bias-extension response of the filament-printed specimen is qualitatively and quantitatively analogous to that of its SLS counterpart, with a clearly identifiable bending-dominated initial branch followed by a strongly nonlinear stretching-dominated regime. Moreover, the compression test indicates that the new hinge effectively postpones the onset of transverse instability, which is the main weakness of the conventional pin-based hinge of Figure 1.

The calibrated numerical model reproduces the bias-extension curve with very good accuracy along the entire loading range, using only the two stiffness parameters K_e and K_b and following a sequential, decoupled calibration strategy in which K_b is identified from the initial bending-dominated branch and K_e from the late stretching-dominated branch. The fact that no torsional contribution is needed in the energy ($K_s = 0$) provides a direct quantitative confirmation of the near-frictionless character of the proposed hinges. Fourth, the same calibrated parameter set, when used to simulate the compression branch, reproduces the experimental curve up to a slight systematic offset that has been tentatively attributed to a residual stiffening of the fibers induced by the prior bending undergone during the bias-extension test; a definitive assessment of this hypothesis requires dedicated cyclic tension–compression tests, which are left to a future investigation.

It should be stressed that the experimental campaign of the present work relies on a single specimen, tested sequentially in bias-extension and then in compression; the study is therefore a proof-of-concept rather than a statistical characterization. A statistically significant campaign on at least three independently tested specimens, a compression test on a virgin specimen, and, more generally, cyclic tension–compression tests with controlled loading histories, are required to consolidate the present findings and are left to future investigations. In the same spirit, a direct comparative measurement of the friction on a single pivot (conventional versus new design) and a parametric study of the influence of the internal-gap size on the pivot behavior would provide further, more stringent evidence, and are also indicated as future work.

These findings open several directions for future work. The most natural extension consists in performing dedicated buckling and post-buckling simulations of the compressed specimen, in order to quantify the gain in critical load with respect to conventional designs; to this aim, the formulations developed in [52], dealing with the interplay between first and second gradient energies in fiber-reinforced sheets, and the objective minimal-constraint formulation for elastic articulated structures of [53] together with the updated Lagrangian Bézier finite-element formulation for slender beams of [54] appear to be particularly well suited. Likewise, isogeometric analysis, which has been shown to be very efficient in the modeling of strongly curved beams [55] and to outperform classical finite elements over the whole spectrum of Timoshenko beam responses [56], represents a promising numerical framework for the simulation of the proposed pantographic lattices under large deformations.

From a continuum mechanics perspective, the present results should be read in the broader context of the recent literature on pantographic metamaterials and generalized elastic media [57–62]: the asymptotic micro-macro identification of [57], the second-gradient one-dimensional continuum formulation of [58], the comprehensive review of inverse problems for generalized elastic media in [60] and the experimental procedure for the identification of the strain-gradient characteristic length proposed in [61] together define the theoretical and experimental framework within which the present hinge concept should be further investigated.

As discussed in Section 5.2, the role played by the hinges in a pantographic lattice admits a direct counterpart in fiber-reinforced composites, where it is played by the in-plane shear stiffness of a compliant embedding matrix; this analogy is, to our knowledge, an original conceptual contribution of the present work. Finally, the pantographic micro-architecture offers a promising strategy for enhancing composite materials [63] by optimizing the placement of inclusions within the matrix. The grid-like pattern of parallel fibers interconnected by hinges naturally facilitates a more uniform dispersion of inclusions, minimizing stress concentrations and yielding composites that are less fragile and more efficient in load transfer. Multi-filament 3D printing, combined with hinge designs of the type proposed here, paves the way for the practical fabrication of such advanced, high-performance composite materials.

Declaration of interests

The authors do not work for, advise, own shares in, or receive funds from any organization that could benefit from this article, and have declared no affiliations other than their research organizations.

References

[1] F. dell'Isola, D. Steigmann and A. Della Corte, "Synthesis of fibrous complex structures: designing microstructure to deliver targeted macroscale response", *Appl. Mech. Rev.* **67** (2015), no. 6, article no. 060804.

[2] M. Spagnuolo and A. M. Cazzani, "Contact interactions in complex fibrous metamaterials", *Contin. Mech. Thermodyn.* **33** (2021), no. 4, pp. 1873–1889.

[3] L. Murcia Terranova, "Planar one-dimensional continua whose energy depends on the gradient of curvature: an overview of their applications in metamaterials design", *Math. Mech. Complex Syst.* **13** (2025), no. 2, pp. 127–166.

[4] E. Barchiesi, M. Spagnuolo and L. Placidi, "Mechanical metamaterials: a state of the art", *Math. Mech. Solids* **24** (2019), no. 1, pp. 212–234.

[5] A. Carcaterra, F. dell'Isola, R. Esposito and M. Pulvirenti, "Macroscopic description of microscopically strongly inhomogenous systems: a mathematical basis for the synthesis of higher gradients metamaterials", *Arch. Ration. Mech. Anal.* **218** (2015), no. 3, pp. 1239–1262.

[6] C. Boutin, F. D'Annibale, C. Pancella and I. Giorgio, "On the mechanical behavior of elastic crenelated beams", *J. Appl. Mech.* **93** (2026), no. 9, article no. 091004.

[7] I. Giorgio and D. Del Vescovo, "Energy-based trajectory tracking and vibration control for multilink highly flexible manipulators", *Math. Mech. Complex Syst.* **7** (2019), no. 2, pp. 159–174.

[8] N. L. Rizzi, P. Seppecher and F. dell'Isola, "A third-gradient 1D continuum obtained via asymptotic expansion from a micro-structure obtained constraining a sequence of modified Harts antiparallelograms", *Math. Mech. Solids* (2026).

[9] F. dell'Isola, S. Moschini and E. Turco, "Towards the synthesis of planar beams whose deformation energy depends on the third gradient of displacement", *Math. Mech. Complex Syst.* **12** (2024), no. 4, pp. 573–597.

[10] L. M. Terranova, E. Turco, A. Misra and F. dell'Isola, "Computational identification of double-bending stiffness: from Zigzagged Articulated Parallelograms with Articulated Braces (ZAPAB) structures to pure-curvature gradient planar inextensible 1D continua", *C. R. Méc.* **353** (2025), no. G1, pp. 647–672.

[11] S. Moschini, L. Murcia Terranova and F. D'Annibale, "Kinematics of zigzagged articulated parallelograms with articulated braces (ZAPAB) mechanisms", *Math. Mech. Complex Syst.* **13** (2025), no. 4, pp. 471–500.

[12] J.-J. Alibert, P. Seppecher and F. dell'Isola, "Truss modular beams with deformation energy depending on higher displacement gradients", *Math. Mech. Solids* **8** (2003), no. 1, pp. 51–73.

[13] P. Seppecher, J.-J. Alibert and F. dell'Isola, "Linear elastic trusses leading to continua with exotic mechanical interactions", *J. Phys.: Conf. Ser.* **319** (2011), no. 1, article no. 012018.

[14] F. dell'Isola, I. Giorgio, M. Pawlikowski and N. L. Rizzi, "Large deformations of planar extensible beams and pantographic lattices: heuristic homogenization, experimental and numerical examples of equilibrium", *Proc. R. Soc. A: Math. Phys. Eng. Sci.* **472** (2016), no. 2185, article no. 20150790-1-23.

[15] R. Afshar and B. E. Abali, "Temporal nonlocality for polymeric metamaterials by means of fractional rheological models", *Math. Mech. Complex Syst.* **14** (2026), no. 3, pp. 341–354.

[16] A. Ciallella, I. Giorgio, E. Barchiesi, et al., "A 3D pantographic metamaterial behaving as a mechanical shield: experimental and numerical evidence", *Mater. Des.* **237** (2024), article no. 112554.

[17] M. Laudato, L. Manzari, D. Scerrato, P. Göransson and I. Giorgio, "Spectral properties of 2D pantographic metamaterial: experimental results", *Mech. Res. Commun.* **109** (2020), article no. 103613.

[18] M. Laudato and E. Barchiesi, "Non-linear dynamics of pantographic fabrics: modelling and numerical study", in *Wave Dynamics, Mechanics and Physics of Microstructured Metamaterials*, Springer: Cham, 2019, pp. 241–254.

[19] S. R. Eugster, "Numerical analysis of nonlinear wave propagation in a pantographic sheet", *Math. Mech. Complex Syst.* **9** (2022), no. 3, pp. 293–310.

[20] A. Ciallella, I. Giorgio, S. R. Eugster, N. L. Rizzi and F. dell'Isola, "Generalized beam model for the analysis of wave propagation with a symmetric pattern of deformation in planar pantographic sheets", *Wave Motion* **113** (2022), article no. 102986.

[21] M. C. Porcu, M. Buitrago, P. A. Calderón, M. Garau, M. F. Cocco and J. M. Adam, "Robustness-based assessment and monitoring of steel truss railway bridges to prevent progressive collapse", *J. Construct. Steel Res.* **226** (2025), article no. 109200.

[22] I. Giorgio, A. Ciallella and D. Scerrato, "A study about the impact of the topological arrangement of fibers on fiber-reinforced composites: some guidelines aiming at the development of new ultra-stiff and ultra-soft metamaterials", *Int. J. Solids Struct.* **203** (2020), pp. 73–83.

[23] I. Giorgio, F. dell'Isola and D. J. Steigmann, "Second-grade elasticity of three-dimensional pantographic lattices: theory and numerical experiments", *Contin. Mech. Thermodyn.* **36** (2024), no. 5, pp. 1181–1193.

[24] A. Ciallella, F. D'Annibale, D. Del Vescovo and I. Giorgio, "Deformation patterns in a second-gradient lattice annular plate composed of "Spira mirabilis" fibers", *Contin. Mech. Thermodyn.* **35** (2023), no. 4, pp. 1561–1580.

[25] G. A. Maugin, "Generalized continuum mechanics: what do we mean by that?", in *Mechanics of Generalized Continua. Advances in Mechanics and Mathematics* (G. Maugin and A. Metrikine, eds.), vol. 21, Springer: New York, 2010, pp. 3–13.

[26] F. dell'Isola, G. Sciarra and S. Vidoli, "Generalized Hooke's law for isotropic second gradient materials", *Proc. R. Soc. A: Math. Phys. Eng. Sci.* **465** (2009), no. 2107, pp. 2177–2196.

[27] F. dell'Isola, P. Seppecher, L. Placidi, E. Barchiesi and A. Misra, *Discrete and Continuum Models for Complex Metamaterials*, Cambridge University Press: Cambridge, 2020, p. 327.

[28] B. E. Abali and H. Yang, "Parameter determination of metamaterials in generalized mechanics as a result of computational homogenization", in *Advanced Problems in Mechanics. APM 2019. Lecture Notes in Mechanical Engineering* (A. K. A. D. Indeitsev, ed.), Springer: Cham, 2019, pp. 22–31.

[29] A. Misra, L. Placidi and D. Scerrato, "A review of presentations and discussions of the workshop Computational Mechanics of Generalized Continua and Applications to Materials with Microstructure that was held in Catania 29–31 October 2015", *Math. Mech. Solids* **22** (2017), no. 9, pp. 1891–1904.

[30] F. dell'Isola, S. R. Eugster, R. Fedele and P. Seppecher, "Second-gradient continua: from Lagrangian to Eulerian and back", *Math. Mech. Solids* **27** (2022), no. 12, pp. 2715–2750.

[31] L. Placidi, F. Di Girolamo and R. Fedele, "Variational study of a Maxwell–Rayleigh-type finite length model for the preliminary design of a tensegrity chain with a tunable band gap", *Mech. Res. Commun.* **136** (2024), article no. 104255.

[32] Y. Rahali, I. Giorgio, J. F. Ganghoffer and F. dell'Isola, "Homogenization à la Piola produces second gradient continuum models for linear pantographic lattices", *Int. J. Eng. Sci.* **97** (2015), pp. 148–172.

[33] B. Desmorat, M. Spagnuolo and E. Turco, "Stiffness optimization in nonlinear pantographic structures", *Math. Mech. Solids* **25** (2020), no. 12, pp. 2252–2262.

[34] I. Giorgio, "Lattice shells composed of two families of curved Kirchhoff rods: an archetypal example, topology optimization of a cycloidal metamaterial", *Contin. Mech. Thermodyn.* **33** (2021), no. 4, pp. 1063–1082.

[35] J. Harsch, G. Ganzosch, E. Barchiesi, A. Ciallella and S. R. Eugster, "Experimental analysis, discrete modeling and parameter optimization of SLS-printed bi-pantographic structures", *Math. Mech. Solids* **27** (2022), no. 10, pp. 2201–2217.

[36] F. Gutmann, M. Stilz, S. Patil, F. Fischer, K. Hoschke, G. Ganzenmüller and S. Hiermaier, "Miniaturization of non-assembly metallic pin-joints by LPBF-based additive manufacturing as perfect pivots for pantographic metamaterials", *Materials* **16** (2023), no. 5, article no. 1797.

[37] A. Özen, G. Ganzosch, E. Barchiesi, D. W. Auhl and W. H. Müller, "Investigation of deformation behavior of PETG-FDM-printed metamaterials with pantographic substructures based on different slicing strategies", *Compos. Adv. Mater.* **30** (2021), article no. 26349833211016477.

[38] M. De Angelo, M. Spagnuolo, F. D'Annibale, et al., "The macroscopic behavior of pantographic sheets depends mainly on their microstructure: experimental evidence and qualitative analysis of damage in metallic specimens", *Contin. Mech. Thermodyn.* **31** (2019), no. 4, pp. 1181–1203.

[39] M. Spagnuolo, P. Peyre and C. Dupuy, "Phenomenological aspects of quasi-perfect pivots in metallic pantographic structures", *Mech. Res. Commun.* **101** (2019), article no. 103415.

[40] G. Sanna, M. Pistis, I. Giorgio, V. A. Eremeyev and M. Spagnuolo, "New hinge design for fibrous metamaterial enables for filament 3D printing", *Mech. Res. Commun.* **148** (2025), article no. 104452.

[41] M. Spagnuolo, V. A. Eremeyev, F. D'Annibale and F. Hild, "Rescaling and mesoshear deformations of lattice metamaterials", *Int. J. Solids Struct.* **315** (2025), article no. 113349.

[42] M. Spagnuolo, "Circuit analogies in the search for new metamaterials: phenomenology of a mechanical diode", in *Nonlinear Wave Dynamics of Materials and Structures* (H. Altenbach, V. A. Eremeyev, I. Pavlov and A. Porubov, eds.), Springer: Cham, Switzerland, 2020, pp. 411–422.

[43] M. Spagnuolo and D. Scerrato, "The mechanical diode: on the tracks of James Maxwell employing mechanical–electrical analogies in the design of metamaterials", in *Developments and Novel Approaches in Biomechanics and Metamaterials* (B. E. Abali and I. Giorgio, eds.), Springer: Cham, 2020, pp. 459–469.

[44] F. dell'Isola, M. Cuomo, L. Greco and A. Della Corte, "Bias extension test for pantographic sheets: numerical simulations based on second gradient shear energies", *J. Eng. Math.* **103** (2017), no. 1, pp. 127–157.

[45] M. Spagnuolo, "Symmetrization of mechanical response in fibrous metamaterials through micro-shear deformability", *Symmetry* **14** (2022), no. 12, article no. 2660.

[46] M. Spagnuolo, K. Barcz, A. Pfaff, F. dell'Isola and P. Franciosi, "Qualitative pivot damage analysis in aluminum printed pantographic sheets: numerics and experiments", *Mech. Res. Commun.* **83** (2017), pp. 47–52.

[47] F. dell'Isola, T. Lekszycki, M. Pawlikowski, R. Grygoruk and L. Greco, "Designing a light fabric metamaterial being highly macroscopically tough under directional extension: first experimental evidence", *Z. Angew. Math. Phys.* **66** (2015), pp. 3473–3498.

[48] M. Cuomo, F. dell'Isola and L. Greco, "Simplified analysis of a generalized bias test for fabrics with two families of inextensible fibres", *Z. Angew. Math. Phys.* **67** (2016), no. 3, article no. 61.

[49] A. Ciallella, D. Pasquali, M. Gołaszewski, F. D'Annibale and I. Giorgio, "A rate-independent internal friction to describe the hysteretic behavior of pantographic structures under cyclic loads", *Mech. Res. Commun.* **116** (2021), article no. 103761.

[50] A. Ciallella, D. Pasquali, F. D'Annibale and I. Giorgio, "Shear rupture mechanism and dissipation phenomena in bias-extension test of pantographic sheets: numerical modeling and experiments", *Math. Mech. Solids* **27** (2022), no. 10, pp. 2170–2188.

[51] K. Benyahi, Y. Bouafia, M. S. Kachi and S. Barboura, "Prediction of effective mechanical properties and development of damage model for inclusion composite materials", *Int. J. Damage Mech.* (2026).

[52] M. Cuomo, F. dell'Isola, L. Greco and N. L. Rizzi, "First versus second gradient energies for planar sheets with two families of inextensible fibres: investigation on deformation boundary layers, discontinuities and geometrical instabilities", *Compos. B: Eng.* **115** (2017), pp. 423–448.

[53] L. Greco, D. Castello and M. Cuomo, "An objective minimal constraint formulation for the analysis of elastic articulated structures", *Comput. Struct.* **305** (2024), article no. 107571.

[54] L. Greco, M. Cuomo, D. Castello and A. Scrofani, "An updated Lagrangian Bézier finite element formulation for the analysis of slender beams", *Math. Mech. Solids* **27** (2022), no. 10, pp. 2110–2138.

[55] A. Cazzani, M. Malagù, E. Turco and F. Stochino, "Constitutive models for strongly curved beams in the frame of isogeometric analysis", *Math. Mech. Solids* **21** (2016), no. 2, pp. 182–209.

[56] A. Cazzani, F. Stochino and E. Turco, "An analytical assessment of finite element and isogeometric analyses of the whole spectrum of Timoshenko beams", *ZAMM Z. Angew. Math. Mech.* **96** (2016), no. 10, pp. 1220–1244.

[57] C. Boutin, F. dell'Isola, I. Giorgio and L. Placidi, "Linear pantographic sheets: asymptotic micro-macro models identification", *Math. Mech. Complex Syst.* **5** (2017), no. 2, pp. 127–162.

[58] E. Barchiesi, S. R. Eugster, L. Placidi and F. dell'Isola, "Pantographic beam: a complete second gradient 1D-continuum in plane", *Z. Angew. Math. Phys.* **70** (2019), no. 5, article no. 135.

[59] Y. Rahali, V. A. Eremeyev and J.-F. Ganghoffer, "Surface effects of network materials based on strain gradient homogenized media", *Math. Mech. Solids* **25** (2020), no. 2, pp. 389–406.

[60] R. Fedele, L. Placidi and F. Fabbrocino, "A review of inverse problems for generalized elastic media: formulations, experiments, synthesis", *Contin. Mech. Thermodyn.* **36** (2024), no. 6, pp. 1413–1453.

[61] N. Rezaei, J. Riesselmann, A. Misra, D. Balzani and L. Placidi, "A procedure for the experimental identification of the strain gradient characteristic length", *Z. Angew. Math. Phys.* **75** (2024), no. 3, article no. 80.

[62] V. A. Eremeyev, "Instability of the third-gradient beam", *Acta Mech.* (2026).

[63] F. Stochino, A. Alibeigibeni, M. Zucca, M. Valdes, G. Concu, M. Simoncelli, M. A. Pisani and C. Bernuzzi, "Mechanical behavior of composite slabs with recycled concrete aggregates: a preliminary study", *Structures* **70** (2024), article no. 107838.